Joint segmentation of anatomical and functional images: Applications in quantification of lesions from PET, PET-CT, MRI-PET, and MRI-PET-CT images

Ulas Bagci [a,b,*], Jayaram K. Udupa [c], Neil Mendhiratta [b,d], Brent Foster [b], Ziyue Xu [b], Jianhua Yao [b], Xinjian Chen [e], Daniel J. Mollura [a,b]

[a] Center for Infectious Diseases Imaging, National Institutes of Health, Bethesda, MD, United States
[b] Department of Radiology and Imaging Sciences, National Institutes of Health, Bethesda, MD, United States
[c] Department of Radiology, University of Pennsylvania, Philadelphia, PA, United States
[d] NYU School of Medicine, New York City, NY, United States
[e] School of electronics and Information Engineering, Soochow University, China

ARTICLE INFO

ABSTRACT

We present a novel method for the joint segmentation of anatomical and functional images. Our proposed methodology unifies the domains of anatomical and functional images, represents them in a product lattice, and performs simultaneous delineation of regions based on random walk image segmentation. Furthermore, we also propose a simple yet effective object/background seed localization method to make the proposed segmentation process fully automatic. Our study uses PET, PET-CT, MRI-PET, and fused MRI-PET-CT scans (77 studies in all) from 56 patients who had various lesions in different body regions. We validated the effectiveness of the proposed method on different PET phantoms as well as on clinical images with respect to the ground truth segmentation provided by clinicians. Experimental results indicate that the presented method is superior to threshold and Bayesian methods commonly used in PET image segmentation, is more accurate and robust compared to the other PET-CT segmentation methods recently published in the literature, and also it is general in the sense of simultaneously segmenting multiple scans in real-time with high accuracy needed in routine clinical use.

Published by Elsevier B.V.

1. Introduction

Magnetic Resonance Imaging (MRI) and Computed Tomography (CT) are widely utilized imaging modalities providing essential detail on anatomic structures via high spatial and contrast resolution (Bagci et al., 2012a). As a non-invasive functional imaging method at the molecular level, Positron Emission Tomography (PET) images the distribution of biologically targeted radiotracers with high sensitivity. PET images have lower spatial resolution than CT and MRI with very limited anatomical characterization, but provide quantitative information about diseases and structures by collecting emitted photons from a radiotracer localizing to abnormal cells. In the assessment of cancer, and more recently in infectious diseases, PET imaging has allowed quantifying the metabolic characteristics of the lesions by exploiting the unique decay physics of positron-emitting isotopes (Juweid and Cheson, 2006). Several radiotracers have been derived from the isotopes in the develop-

ment of diagnositically useful biologic compounds such as isotopes of oxygen, carbon, nitrogen, and fluorine. Among those isotopes, ^{18}F-fluorodeoxyglucose ($^{18}F − FDG$) is the most commonly used PET radiotracer in the evaluation of several neoplasms as well as in the planning of radiotherapy in various cancers, such as lung and head-neck tumors (Juweid and Cheson, 2006; Brindle, 2007; Shankar et al., 2006). These types of lesions show up regulation of glucose metabolism, and labeling glucose with ^{18}F renders these lesions detectable using PET (Miele et al., 2008). Unless otherwise stated, all the PET images analyzed in this article were obtained using the $^{18}F − FDG$ PET radiotracer.

In vivo characterization and measurement of biologic processes at the cellular and molecular level is assessed by PET imaging; however, anatomical imaging techniques such as MRI or CT are still needed to localize, visualize, and co-evaluate abnormal regions. In other words, since PET images generally lack anatomic context and are of lower spatial resolution, combining unique strengths of functional and anatomical imaging modalities (PET-CT, and more recently MRI-PET (Judenhofer et al., 2008)) has received much attention due to the frequent need for diagnosing and characterizing the disease type accurately. In Fig. 1, we demonstrate an

* Corresponding author at: Department of Radiology and Imaging Sciences, National Institutes of Health, Bethesda, MD, United States.
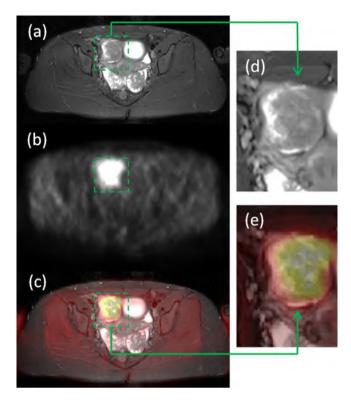E-mail addresses: ulasbagci@gmail.com, ulas.bagci@nih.gov (U. Bagci).

Fig. 1. A patient (aged 28, female) with paragangliomas tumor is shown at (a) MRI, (b) PET, and (c) MRI-PET scans. Note that simultaneous MRI-PET imaging provides anatomical and functional information fused into the same space without needing a registration. Zoomed tumor sites from (a) and (c) are shown in (d) and (e), respectively.

example slice from the MRI-PET scan where cancerous regions in the structural image are shown at (a), corresponding uptake regions at (b), and the fused information at (c), and the display at (a) and (c) is shown zoomed at (d) and (e). Simultaneous imaging with FDG-PET and anatomic MRI shows a hyperintense focus of FDG uptake in the tumor site, and the extent of the tumor can be well defined on the fused image. Similarly, in Fig. 2, we show superior contrast of PET images (middle column), superior spatial resolution of CT images (last column), and fused PET-CT images (first column). It may be very difficult to differentiate normal tissue from abnormal at CT if the PET image is not provided. For example, CT image in the first row shows similar gray level intensity profile for different abnormal regions, but activity levels of those regions are quite different (i.e., 7.25 vs 3.82 maximum standardized uptake value SUV_{max}). We will describe how to measure tissue activity level in the following section.

1.1. Standardized uptake value

Accurate diagnosis and the assessment of treatment response, particularly predicting response during treatment, requires a quantitative assessment of changes in $^{18}F - FDG$ uptake, as a surrogate for glucose metabolism as proposed in the PERCIST framework (Wahl et al., 2009), which is the guideline currently used by clinicians. Various semi-quantitative and quantitative methods such as SUV, tumor to background ratio (TBR), nonlinear regression techniques, total lesion evaluation (TLE), and the Patlak-derived methods are currently undergoing extensive exploration for obtaining accurate quantitative information from metabolic activities (Basu et al., 2011). However, there is no clear consensus as to which of them is clinically applicable and provides optimal measurements. SUV is perhaps the most widely used method for quantification of lesions as it gives a physiologically relevant measurement of cel-

lular metabolism. SUV represents the $^{18}F - FDG$ uptake within a lesion, measured over a certain time interval after $^{18}F - FDG$ administration, and normalized to the dosage of $^{18}F - FDG$ injected and a factor (such as body weight, lean body weight, or body surface area) that takes into account distribution through the body (Boellaard et al., 2004). SUV normalized to body weight is given by

$$SUV = \frac{AC_{ROI}^T \ (Bq/ml)}{Injected \ Dose \ (Bq)/Body \ Weight \ (kg)} \tag{1}$$

where AC_{ROI}^T denotes radioactivity concentration for a given region of interest (ROI) at time T, and it can be measured directly from a ROI drawn on a reconstructed PET image calibrated to Bq/ml as,

$$AC_{ROI}^T = \frac{Image \ Intensity}{Image \ Scale \ Factor}, \tag{2}$$

and

$$Injected \ Dose \ (Bq) = (actual \ activity$$
$$* \ dose \ calibration \ factor). \tag{3}$$

As shown in Eq. (1), SUV is a simplified measure affected by many factors such as body weight (or body surface area), injected dose, and calibration constant. Detailed explanations of these factors along with further variables such as image reconstruction parameters can be found in the review paper (Fletcher et al., 2008).

SUV measurement can also detect clinically relevant metabolic changes when no or minimal changes are observed by structural imaging (Cypess et al., 2009; Thie, 2004), but it is easily affected by many factors including partical volume effects. Partial volume calculation requires segmentation of the actual lesion to correct SUV measurements. In addition, SUVs alone are not enough in PET-CT or MRI-PET imaging to diagnose, characterize, and stage disease, because anatomic boundaries of the corresponding structural images (CT or MRI) are also needed. For instance, due to its low resolution, PET images do not clearly indicate the lesion's size or location or the involvement of any critical anatomical structures that would alter the treatment strategy. The use of hybrid imaging techniques (PET-CT and MRI-PET) are preferred in order to provide higher accuracy in evaluating lesions' morphological and metabolic characteristics simultaneously. As a result, diagnostic sensitivity and specificity achieved are higher in hybrid imaging modalities than either modality alone (Judenhofer et al., 2008; Evanko, 2008).

While all these processes require precise segmentation of both functional and anatomical images, most segmentation methods in PET imaging are based on thresholding techniques with no clear consensus on the selection of an optimal threshold value for delineation. Hence, an accurate diagnosis or assessment of treatment response in radiotherapy procedures is very difficult as any small change in SUV measurement and morphological properties, such as metabolic activity or gross lesion volumes, can easily affect the decision process. Region delineation must be performed meticulously and accurately in both structural and functional images for the following reasons: (1) Errors in segmentation can distort the SUV calculations by altering the region's margins, (2) manual or semi-automated mechanisms of segmentation can be inefficient and suffer from unacceptable inter-observer variance and the variabilities in the anatomic image, and (3) using CT or MRI for segmenting lesions that are quantitatively measured on PET can overlook and exclude other important quantitative data such as texture features in PET images. Because of all these reasons, we aim to construct an automated robust segmentation method that simultaneously unifies anatomic and functional information with high precision and accuracy while being fast and efficient enough to be used in routine clinical applications. The proposed method can be especially useful in quantifying lesions characterized by
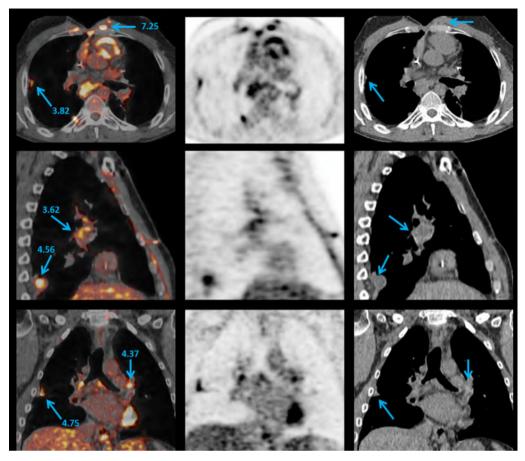
Fig. 2. PET-CT (first column), PET (second column), and CT (third column) images are shown in axial, sagittal, and coronal view in the first, second, and third rows, respectively. SUV_{max} of different uptake regions is indicated by blue arrows. CT images usually do not show anatomically abnormal appearance even though high SUV_{max} is observed at PET.

fuzzy boundaries and low contrast from surrounding normal structures.

1.2. Related works

Due to the nature of the PET images (i.e., fuzzy boundaries of uptake regions, low spatial resolution, and high contrast), most of the PET image segmentation methods are based on thresholding techniques (Nestle et al., 2006; Drever et al., 2006; Erdi et al., 1997; Drever et al., 2007; van Dalen et al., 2007; Jentzen et al., 2007; Van Baardwijk et al., 2007; Vees et al., 2009). These techniques may use either fixed or adaptive thresholds based on expert interaction or phantom simulations. In fixed thresholding, a clinically accepted value of $SUV = 2.5$ or 40% of the SUV_{max} (i.e., maximum SUV of a predefined region) is used to delineate lesions from the background for a given region of interest (ROI) drawn manually (Nestle et al., 2006). In adaptive thresholding methods, a more optimal thresholding level is searched by examining class uncertainties (Otsu, 1979), by building realistic phantoms (Matheoud et al., 2011; Davis et al., 2006; Brambilla et al., 2008; Schaefer et al., 2008), by applying iterative thresholding based on scanner hardware properties (Drever et al., 2007; van Dalen et al., 2007; Jentzen et al., 2007), or by incorporating local approaches into the threshold selection process (Erdi et al., 2002; Bradley et al., 2004; Ciernik et al., 2005; Koshy et al., 2005). It has been shown in various studies (Fahey et al., 2010) that the lack of optimal threshold levels in these approaches prevents accurate and robust delineation of lesions from the background. Expert demarcation is also unreliable as demonstrated by consistently low inter- and intra-operator agreement (Fox et al., 2005; Fiorino et al., 1998; Erasmus et al.,

2003; Bagci et al., 2011). It is also worth noting that some of the fixed thresholding methods that extract analytical thresholding equations from digital or physical phantoms can have better accuracy in delineating lesions compared to other fixed and adaptive thresholding methods. However, these methods are often restricted to the delineation of lesions larger than 4 mL, and a prior estimation of lesion volume from structural imaging is usually required. More details on threshold based segmentation methods for PET images and a comparative evaluation of the methods can be found in (Boudraa and Zaidi, 2006; Zaidi and El Naqa, 2010; Prieto et al., 2012; Schinagl et al., 2007).

Similar to the thresholding approaches, Fuzzy-C-Means (FCM) (Zaidi et al., 2002; Belhassen and Zaidi, 2010), Fuzzy Locally Adaptive Bayesian (FLAB) (Hatt et al., 2009), and iterative thresholding methods (ITM) (Jentzen et al., 2007) are extensively used in PET image segmentation because the boundary representation in these approaches is well suited for the fuzzy nature of the lesion boundaries. For instance, FLAB is based on a Bayesian statistical model where a finite number of fuzzy levels is used to label voxels within a ROI as belonging to more than two classes (i.e., in addition to background and foreground classes). In ITM, on the other hand, threshold volume curves adapted from a specific PET scanner at varying levels of source-to-background ratios (SBRs) are used to determine an analytic expression to estimate a threshold level for delineation. It is an iterative process and in each iteration, the threshold level is updated until there is no significant change in the threshold level observed. Although all these methods can segment circular uptake regions with the help of precisely defined ROIs, the accuracy of the ITM, FLAB, and FCM delineation algorithms is limited to only large lesions of simple shape; uptake

regions of complex shape are not easy to delineate. Specifically, FLAB needs a significant number of background and foreground voxels within the manually drawn ROIs to provide reliable statistical estimation of voxel labels. The accuracy, robustness, and reproducibility of these methods are suspect in more difficult cases.

Apart from the approaches described above, region growing (Li et al., 2008; Day et al., 2009), gradient based (Geets et al., 2007), level set and active contours (Kanakatte et al., 2008; El Naqa et al., 2007), and more recently graph based approaches (Bagci et al., 2011; Yang and Grigsby, 2012) are also actively in use for certain clinical applications. In most of these approaches, user defined foreground and background seeds, or ROIs are necessary to initiate and restrict the segmentation bounds. Although these advanced image segmentation methods have been touted to provide better accuracy compared to thresholding methods, they have many shortcomings preventing them from routine clinical use. For instance, in region growing approaches (Li et al., 2008; Day et al., 2009), segmentation of heterogeneous structures is often erroneous due to the main assumption that the region to be segmented is sufficiently homogeneous. Furthermore, gradient and contour based methods require smooth regions with reliable edge information (Geets et al., 2007; Kanakatte et al., 2008; El Naqa et al., 2007). However, PET scans produce low resolution and noisy images in which pre-processing methods are applied to reduce noise effects. Spectral clustering and graph based segmentation have been proposed in (Bagci et al., 2011; Yang and Grigsby, 2012) to alleviate the difficulty of segmenting complex boundaries in low contrast images. These approaches are promising and have been shown to be superior to the existing thresholding approaches in PET image segmentation.

All approaches reported above are formulated without incorporating corresponding anatomical information (i.e., CT or MRI) into the segmentation process (excluding phantom based studies where anatomical volume information may be estimated to help in choosing a near-optimal threshold). In clinical use, it is highly desirable to have both functional and structural quantifiable information in a single scan so the disease can be both identified and localized, potentially resulting in an earlier diagnosis and more effective treatment plan. In parallel to the developments in multi-modal scanners (PET-CT and MRI-PET), there have been recent attempts in the literature trying to bring the usefulness of integrating anatomical and functional information into a common place for separating tumor tissues from normal structures (Yu et al., 2009; Han et al., 2011; Bagci et al., 2012b). In (Yu et al., 2009), textural features from CT images were used to distinguish cancerous tissue types, and PET information was incorporated into this knowledge. However, long execution times and sub-optimal image segmentation solutions were the main concern of the approach. A joint PET-CT image segmentation method was proposed recently in (Han et al., 2011), where a Markov Random Field algorithm was formulated on a graph. The method requires user interaction, and it was used only in images from head and neck with large tumors. Its performance in small uptake regions was not assessed. Another shortcoming of the approach was due to the potentially unrealistic assumption that there is a one-to-one correspondence between PET and CT delineations. For example, lesions may have smaller uptake regions (on PET images) compared to outlines of lesions in CT images because of the functional or metabolic characteristics of the tumor.

In (Bagci et al., 2012b), we considered all these issues and proposed a co-segmentation method which is driven by the uptake regions from PET in finding the correct anatomical boundaries in the corresponding CT images. Although the underlying mathematics and methods of the proposed co-segmentation method in our approach are completely different from (Han et al., 2011), the intuitions are quite similar. This paper is a substantial and full extension of our preliminary report which appeared in the proceedings of MICCAI 2012 (Bagci et al., 2012b), In this paper, we apply the proposed simultaneous segmentation algorithm to PET-CT and MRI-PET body images and examine the correspondence issue between functional and anatomic structures and its intuitive adaptation to the proposed segmentation algorithm. We generalize the algorithm for delineating more than two fused images simultaneously (i.e., CT fused into MRI-PET scans). We extend the random walk method for jointly delineating multiple objects from multiple image modalities by unifying graph representation of each image modality in a single product lattice. The method allows users to adapt the algorithm to cases where one-to-one correspondence between anatomical and functional structures is not satisfied. The method also offers automated object detection via *interesting uptake region (IUR)* algorithm to avoid users having to provide seeds.

The rest of the manuscript is organized as follows. In Section 2, we first describe the delineation methods using random walk for single and multiple images, and propose a method for the automatic detection of uptake regions based on the PET image. In Section 3, we investigate the performance of the co-segmentation algorithm for clinical cases with PET, PET-CT, MRI-PET, and fused MRI-PET-CT images. We also demonstrate the precision and accuracy of the delineation algorithm in phantom data. We conclude the paper with a summary of our findings in Section 4.

2. Methods

We represent an image as *graph* such that *nodes* and *edges* of the graph are defined by space elements (*spels* for short) of the image, and edges of the graph are assigned with cost values corresponding to spel adjacency. Graph based segmentation methods partition the nodes into two disjoint subsets representing the object and background. This process can be accomplished by finding the minimum cost/energy among all possible cut scenarios in the graph (as in graph-cut algorithms) or optimizing some form of energy combining boundary regularization with regularization of regional properties of segments (Han et al., 2011). However, a common problem with these approaches is the "small cut" or shrinking behavior (i.e., tendency to have small segmentations due to minimizing the sum of edge weights in the cut) and leakages (Chen et al., 2011; Kolmogorov and Boykov, 2005; Chen and Bagci, 2011; Chen et al., 2010). As a possible solution to this behavior, the random walk algorithm was proposed which is more efficient than the conventional graph-cut algorithms in terms of handling ambiguities among object boundaries (i.e., weak edges among objects) and more accurate segmentation in noisy and low contrast images (Bagci et al., 2011; Grady, 2006). Since PET images are of low spatial resolution, and weak boundaries often exist in anatomical images, random walk is a natural choice for the simultaneous segmentation of PET and anatomical images (CT and MRI). In this study, not only we demonstrate that random walk algorithm is superior to other state of the art algorithms in segmenting uptake regions from PET images, but we also *reformulate* random walk as a co-segmentation algorithm for delineating functional and anatomical images simultaneously and providing globally optimum segmentation results. Furthermore, to create a fully automated framework, we propose an automated seed localization framework by identifying IUR in PET images, a method, using these regions, to identify foreground and background seeds, and a method of propagating the detected background and foreground seeds to the corresponding anatomical images prior to the initiation of the segmentation process. Alternatively, one may use a conventional interactive seeding procedure to initiate segmentation (Bagci et al., 2011).

2.1. Automated random walk co-segmentation

Let a connected and un-directed graph G be represented as a pair $G = (V,E)$ with nodes $v \in V$ and edges $e \in E \subseteq V \times V$. Conventionally, a node v_i is said to be a neighbor of another node v_j if they are connected by an edge e_{ij} in G. Each edge is weighted by w_{ij}. Since the graph is assumed to be connected and un-directed: $w_{ij} = w_{ji}$. By following the recommendation in (Grady, 2006), we construct the weighting functions for functional and anatomical image modalities separately as

$$w_{ij}^{PET} = exp\left(-\beta^{PET}\left(I_i^{PET} - I_j^{PET}\right)^2\right), \tag{4}$$

$$w_{ij}^{\Omega} = exp\left(-\beta^{\Omega}\left(I_i^{\Omega} - I_j^{\Omega}\right)^2\right). \tag{5}$$

where I_i indicates the intensity at spel i, β represents a weighting factor, and Ω indicates the anatomical imaging modality, which is either CT or MRI, i.e., $\Omega \in \{CT, MRI\}$. Note that PET and Ω images are obtained from the same scanner in the same scanning session; therefore they are in registration by the nature of the hybrid scanner and there is a one-to-one *spel correspondence* between them. Conventionally, the desired random walker probabilities have the same solution as the combinatorial Dirichlet problem (Harary, 1994):

$$D[x] = \frac{1}{2}x^T L x, \tag{6}$$

where x denotes the probability (potential) assumed at each node (Grady, 2006), and L represents the combinatorial Laplacian matrix. For each of the functional and anatomical imaging modalities, this matrix can be formulated as:

$$L_{ij}^{\mathcal{X}} = \begin{cases} d_i^{\mathcal{X}} & \text{if } i = j \\ -w_{ij}^{\mathcal{X}} & \text{if } v_i^{\mathcal{X}} \text{and } v_j^{\mathcal{X}} \text{ are adjacent nodes} \\ 0 & \text{otherwise}, \end{cases} \tag{7}$$

where $\mathcal{X}$ is one of the imaging modalities under consideration: $\mathcal{X} \in \{CT, MRI, PET\}$, and d_i is the degree of a vertex considering all edges e_{ij} incident on v_i and is defined as: $d_i = \sum_{e_{ij} \in E} w(e_{ij})$. Moreover, v^{PET} and v^{Ω} are the nodes pertaining to the graph constructed on PET and corresponding Ω images, respectively.

Hyper-graph construction (G^H): Simultaneous segmentation of hybrid images on the graph requires a special representation of both data without loss of information. From graph theory, it is well known that given two graphs and their product as an outcome graph, an edge exists in the product graph *if and only if* an edge exists in both graphs (Harary, 1994). Defining a special graph combining these two graphs, or a hyper-graph, is a natural choice to satisfy this property. Given two graphs $G^{\Omega} = (V^{\Omega}, E^{\Omega})$ and $G^{PET} = (V^{PET}, E^{PET})$, without loss of generality, we define our special product graph as $G^H = (V^H, E^H)$, where H stands for "hybrid". V^{Ω} and V^{PET} have the same number of spels due to one-to-one spel correspondence. G^H has an important property that an edge exists in E^H *if and only if* the corresponding nodes are adjacent in both G^{Ω} and G^{PET}. Thus,

$$V^H = \left\{ \left(v_i^{\Omega}, v_i^{PET}\right) : v_i^{\Omega} \in V^{\Omega} \wedge v_i^{PET} \in V^{PET} \right\},$$
$$E^H = \left\{ \left(\left(v_i^{\Omega}, v_i^{PET}\right), \left(v_j^{\Omega}, v_j^{PET}\right)\right) : \right. \tag{8}$$
$$\left. \left(v_i^{\Omega}, v_j^{\Omega}\right) \in E^{\Omega} \wedge \left(v_i^{PET}, v_j^{PET}\right) \in E^{PET} \right\}.$$

Instead of using a separate implementation of G^{Ω} and G^{PET}, we use the product graph G^H to segment objects simultaneously. Since the critical points of $D[x]$ are assumed to be minima, finding these minima points yields the solution for the random walk probabilities. This requires an updated definition of the combinatorial Laplacian

matrix on the product graph. The combinatorial Laplacian matrix (L^H) of the product graph G^H is defined as:

$$L^H = (L^{\Omega})^{\alpha} \otimes (L^{PET})^{\theta}, \tag{9}$$

where α and θ are constants, $0 \leqslant \alpha, \theta \leqslant 1$, and $\otimes$ denotes direct product. Meanwhile, let x^{Ω} and x^{PET} denote initial probability distributions (i.e., priors) over nodes of G^{Ω} and G^{PET}. Then, the initial probability distribution x^H of the product graph is

$$x^H = (x^{\Omega})^{\zeta} \otimes (x^{PET})^{\eta}, \tag{10}$$

where ζ and η are used to optimize the initial probability distributions subject to the constraint $0 \leqslant \zeta, \eta \leqslant 1$. Performing a random walk on the product graph G^H is equivalent to performing a simultaneous random walk on the graphs G^{Ω} and G^{PET} (Harary, 1994). Therefore, the combinatorial formulation of Dirichlet integral can be updated and re-written as

$$D[x^H] = \frac{1}{2}(x^H)^T L^H x^H = \frac{1}{2}\sum_{e_{ij} \in E^H} w_{ij}^H \left(x_i^H - x_j^H\right)^2, \tag{11}$$

where a combinatorial harmonic function of x^H, satisfying the Laplace equation $\triangledown^2 x^H = 0$, minimizes Eq. (11). We can decompose Eq. (11) by considering prior probabilities and Laplacian matrices of labeled and unlabeled nodes separately as

$$D[x_u^H] = \frac{1}{2}\left[(x^H)_l^T (x^H)_u^T\right]\begin{bmatrix} L_l^H & B \\ B^T & L_u^H \end{bmatrix}\begin{bmatrix} x_l^H \\ x_u^H \end{bmatrix}, \tag{12}$$

where B corresponds to the sub-matrix in the matrix decomposition of L^H. Given the fact that the combinatorial Laplacian matrix L^H is positive semi-definite, critical points of $D[x^H]$ are only the minima; hence, differentiating $D[x^H]$ with respect to prior probability distributions of unlabeled nodes x_u^H and finding the minima yields $L_u^H x_u^H = -B^T x_l^H$, where L_u^H and B are known, and x_l^H is nothing but the prior for labeled node. Solving this equation for every x_u^H completes the binary labeling problem of co-segmentation on the graph G^H.

2.2. Extension to co-segmentation of hybrid images

Owing to the underlying unifying property, the co-segmentation framework is not restricted to segmenting objects from only two modalities. It is possible to co-segment objects from multiple imaging modalities as long as the graph representations of the corresponding imaging modalities exhibit the properties previously mentioned: *including all available graphs in a single product graph requires that an edge exists in the product graph if and only if an edge exists in both graphs*. Assume that M imaging modalities $\Omega \in \{\Omega_1, \Omega_2, \ldots, \Omega_M\}$ are available for the co-segmentation process: $\{\Omega_1 = MRI, \Omega_2 = CT, \Omega_3 = PET, \Omega_4 = SPECT, \Omega_5 = US, \ldots\}$ from the same subject, the same body region, and there is no misregistration such that there is a one-to-one spel correspondence among images. Then, the co-segmentation process can be extended readily to handle simultaneous delineation of objects from $M > 2$ modalities.

One practical application of this extension, also potentially useful in routine clinical use, is the fusion of CT images into MRI-PET hybrid images (i.e., $M = 3$). Since there is no mechanism for obtaining MRI-PET-CT images simultaneously from the same scanner, we need to provide the spel-correspondence between CT and MRI-PET scans via non-linear registration (Bagci and Bai, 2010). Assuming CT scans are obtained in the same day of the MRI-PET scans of the same subject and the same body region, and no significant anatomical and functional changes have been observed between the scans, we can directly construct the hyper-graph $G^F = (V^F, E^F)$ (F stands for "fuse" as below) as

$$V^F = \left\{ \left(v_i^{MRI}, v_i^{CT}, v_i^{PET} \right) : \right.$$
$$\left(v_i^{MRI} \in V^{MRI} \right) \wedge \left(v_i^{CT} \in V^{CT} \right) \wedge \left(v_i^{PET} \in V^{PET} \right) \right\},$$
$$E^F = \left\{ \left(\left(v_i^{MRI}, v_i^{CT}, v_i^{PET} \right), \left(v_j^{MRI}, v_j^{CT}, v_j^{PET} \right) \right) : \right.$$
$$\left(v_i^{MRI}, v_j^{MRI} \right) \in E^{MRI} \wedge \left(v_i^{CT}, v_j^{CT} \right) \in E^{CT} \wedge \left(v_i^{PET}, v_j^{PET} \right) \in E^{PET} \right\}. \tag{13}$$

In this particular extension, we use the term F in the constructed hyper-graph to differentiate from the previous usage of "hybrid" denoted by H in hyper-graph construction of two modalities where functional and anatomical images were directly obtained from the same scanner. Now, on the other hand, we need to fuse CT images into hybrid MRI-PET scans. Similar to the co-segmentation of PET-CT and MRI-PET scans in the previous subsection, the combinatorial Laplacian matrix (L^F) of the product graph G^F can be re-defined as

$$L^F = (L^{CT})^\alpha \otimes (L^{PET})^\theta \otimes (L^{MRI})^\gamma, \tag{14}$$

where α, θ and γ are constants, and $0 \leqslant \alpha, \theta, \gamma \leqslant 1$. Furthermore, initial probability distribution x^F of the product graph can be written as

$$x^F = (x^{MRI})^\xi \otimes (x^{CT})^\zeta \otimes (x^{PET})^\eta, \tag{15}$$

where x^{MRI}, x^{CT} and x^{PET} denote priors over nodes of G^{MRI}, G^{CT} and G^{PET}, respectively. ξ, ζ, and η are used to optimize the initial probability distributions subject to the constraints $0 \leqslant \zeta, \eta, \xi \leqslant 1$. Performing a random walk on the product graph G^F is now equivalent to performing a simultaneous random walk on the graphs G^{MRI}, G^{CT}, and G^{PET} (Harary, 1994).

2.3. Automatic detection of interesting uptake regions (IUR) for seed specification

The goal in seed localization is to define the foreground and background regions in both PET and CT images. An overview of the proposed automated background and foreground seed localization method is sketched in Fig. 3a–d. Briefly, we partition the image into a set of regions such that some of those regions (i.e., IURs) are more similar to each other than to other regions. We accomplish this selection procedure by defining an encoder function $c(\lambda)$, equivalent to thresholding for PET images:

$$c(\lambda) = \begin{cases} 1, & \lambda \in \left[SUV_{max}^{global}/N, SUV_{max}^{global} \right], \\ 0, & \text{otherwise}, \end{cases} \tag{16}$$

where $(N \geqslant 1.5) \in \mathcal{R}$ is a free parameter, and each region identified by the encoding function is considered as an IUR. Once IURs are identified, we set the number of disconnected IURs as a hard constraint (i.e., number of objects to be segmented) on seed localization. The seed localization procedure is as follows:

(i) Both anatomical and functional images are median filtered to smooth the images.
(ii) We find the skin boundary from thresholded anatomical images by using mathematical morphology, i.e., with five iterations of opening followed by closing. We incorporate this anatomic boundary information into the corresponding functional image (black outlines in Fig. 3a–c).
(iii) We find the IURs inside the body region and pertaining to the interval of $[SUV_{max}^{global}/N, SUV_{max}^{global}]$ by using Eq. (16) (Fig. 3d).
(iv) For each IUR, the spels with the maximum SUVs (SUV_{max}^{local}) of that particular IUR are marked as foreground seeds (marked red in Fig. 3a–c). Note that maximum SUV of any IUR (i.e., SUV_{max}^{local}) does not necessarily equal SUV_{max}^{global}.
(v) At each spel, marked as a foreground seed, we explore its neighborhood through searching in 8 directions (Harary, 1994). For all 8-directions starting from each foreground seed, we find locations of the very first spels found with values less than or equal to SUV_{max}^{global}/N within the skin boundary. Those spels are marked as background seeds. Fig. 3b (marked green) illustrates this procedure for a particular foreground seed.
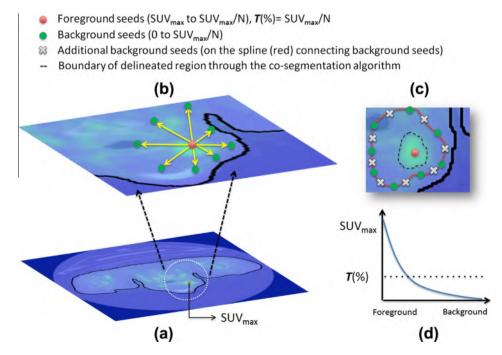

Fig. 3. The concepts of interesting uptake region (IUR) detection and background/foreground seed localization are sketched in (a–d). Green markers are connected by b-splines (c) and additional background seeds (indicated by white markers) are located on the b-splines connecting background seeds (c). The resulting co-segmentation from the localized seeds is shown as a dashed curve in (c). (For interpretation of the references to color in this figure legend, the reader is referred to the web version of this article.)

(vi) We add additional background seeds (marked white in Fig. 3c) into the spels lying in the spline connecting background seeds determined in the previous step. For each foreground seed, we find 8 background seeds due to the search in the 8 directions on the neighborhood.

Note that it may be possible for the same connected component to have more than one foreground seed corresponding to local max. In that case, we still find 8 background seeds for each foreground seed, whereas one may easily constrain the maximum number of foreground seeds for each connected component to a pre-defined value (e.g., maximum 5 foreground seeds per region). Once the foreground and background seeds are localized, random walk algorithm will perform co-segmentation of each IUR by utilizing the seed sets and the fused graph. A pseudo-code for the IUR detection algorithm is the following:

Algorithm 1. Automatic Detection of IURs and Seeding

Input: PET and corresponding structural images: $\mathcal{C}^{PET}$ and $\mathcal{C}^{\Omega}$, a fixed threshold:N(=2.5 by default), morphological iteration: $mIter$ (=5 by default), Morphological structural element: $strel$, maximum number of foreground seeds for each IUR: mfs
Output: Foreground and background seeds as dynamic arrays: $fseeds$, $bseeds$.
1: **Begin**
2:   $\widehat{\mathcal{C}}^{PET} \leftarrow MedianFilt\{\mathcal{C}^{PET}\}, \widehat{\mathcal{C}}^{\Omega} \leftarrow MedianFilt\{\mathcal{C}^{\Omega}\}$
3:   $\widehat{\mathcal{C}}^{\Omega} \leftarrow SmoothingFilt\{\widehat{\mathcal{C}}^{\Omega}\}$
4:   $\mathcal{C}^{temp} \leftarrow MakeBinary\{\widehat{\mathcal{C}}^{\Omega}\}$,// Thresholding on skin body level.
5:   **For** i = 1:$mIter$
6:     $\mathcal{C}^{temp} \leftarrow \mathcal{C}^{temp} \circ strel$,// $\circ$ denotes opening.
7:   **EndFor**
8:   **For** i = 1:$mIter$
9:     $\mathcal{C}^{temp} \leftarrow \mathcal{C}^{temp} \bullet strel$,// $\bullet$ denotes closing.
10: **EndFor**
11:   $\widehat{\mathcal{C}}^{\Omega} \leftarrow \widehat{\mathcal{C}}^{\Omega}.^* \mathcal{C}^{temp}$,//.* denotes masking operation.
12:   $\widehat{\mathcal{C}}^{PET} \leftarrow \widehat{\mathcal{C}}^{PET}.^* \mathcal{C}^{temp}$
13:   $SUV_{max}^{global} \leftarrow \max\{\widehat{\mathcal{C}}^{PET}\}$
14:   Use Eq. (16) to find IURs.// Let nIURs denotes number of IURs.
15:   nIURs $\leftarrow ConnectedComponentImageFilter(\widehat{\mathcal{C}}^{PET})$
16:   **For** i = 1:$nIURs$
17:     **For** j = 1:mfs
18:       $SUV_{max}^{local} \leftarrow \max\{IURs\{i\}\}$
19:       $fseeds\{i\}\{j\} \leftarrow SUV_{max}^{local}$
20:       $IURs\{\max\{IURs\{i\}\} \leftarrow 0$
21:     **EndFor**
22:   **EndFor**
23:   **For** i = 1:$nIURs$
24:     **For** j = 1:mfs
25:       $initialbseeds\{i\}\{j\} \leftarrow Search8Neighbors(fseeds\{i\}\{j\})$
26:       $bseeds\{i\}\{j\} \leftarrow RefineBySplineFit(initialbseeds\{i\}\{j\})$
27:     **EndFor**
28:   **EndFor**
29:   Output $fseeds$ and $bseeds$
30: **End**

---

3. Experiments and results

With IRB approval, we collected 77 image sets from 56 patients. We devised evaluation of our segmentation experiments in four analysis groups: (1) PET segmentation, (2) PET-CT co-segmentation, (3) MRI-PET co-segmentation, and (4) MRI-PET-CT co-segmentation. In accordance with our analysis scenarios, we collected the images retrospectively from the image database in our clinics. For (1), 20 patients with diffusive lung parenchymal diseases, primary lung cancer, metastatic papillary renal cell carcinoma, soft tissue thoracic mass, and lung neoplasm underwent PET scanning. In (2), 15 patients with non-specific infectious lung diseases with observed abnormal imaging patterns (i.e., ground glass opacity (GGO), consolidation, etc.), diffuse large B-cell lymphoma, lymphomatoid granulomatosis, non-necrotizing granulomatous inflammation, and metastatic alveolar soft part sarcoma underwent PET-CT imaging. For (3), 21 patients with Von-Hippel–Lindau diseases, colon cancers, paraganglioma carcinoid tumors, and hederditary leiomyomatosis renal cell cancer have undergone MRI-PET and PET-CT scanning either on the same day or the following day. For MRI-PET-CT co-segmentation (4), it was assumed that there was no significant metabolic and anatomic changes in the object of interest within the duration between scans, and therefore fusion of CT into MRI-PET scans facilitated the conduct of co-segmentation algorithm in more than two modalities. In experiments (1), (2), and (3), there was no need for registering scans as images were obtained simultaneously by the scanner. In (4), we used non-linear deformable registration (i.e., globally smooth locally affine registration) (Bagci and Bai, 2010; Bagci and Bai, 2008; Bagci and Bai, 2007) to provide spel correspondence among images. Scanning parameters and details of the data used in our experiments are listed in Table 1. Note that the imaging parameters for CT, MRI, and PET are native resolutions of the scanners; for visualization and other image processing tasks, a resampling is necessary for spel correspondence.

3.1. Evaluation metrics and observer agreements

To evaluate the accuracy of the segmentation, we use the dice similarity coefficient (DSC) (Dice, 1945) and Hausdorff distance (HD) (Cignoni et al., 1998) with respect to the ground truth (i.e., surrogate truth) constructed through expert's manual delineations. While DSC is a measurement of spatial overlap (in percentage) between segmented object and the ground truth, HD is a shape dissimilarity metric measuring the most mismatched boundary points between the segmented object and the ground truth. High DSC and low HD values indicate high accuracy of the image segmentation method. Assuming the segmented volume and the ground truth are denoted by U_1 and U_2, respectively. DSC is expressed as

$$DSC(U_1, U_2) = 2\frac{|U_1 \cap U_2|}{|U_1| + |U_2|}$$
$$= \frac{2^* TPFV}{(FPVF + TPVF) + (TPVF + FNVF)}, \quad (17)$$

where $TPVF$, $FNVF$, and $FPVF$ indicate true positive, false negative, and false positive volume fractions, respectively. HD, on the other hand, is a metric measuring how boundaries of two segmented objects are in disagreement, expressed as the largest deviation in boundary from each other. Assuming ∂ denotes the boundary of segmented volumes such that $X = \partial U_1$ and $Y = \partial U_2$, then

$$HD(X, Y) = H(\partial U_1, \partial U_2)$$
$$= \max\{\sup_{x \in X} \inf_{y \in Y} d(x, y), \sup_{y \in Y} \inf_{x \in X} d(x, y)\}, \quad (18)$$

where d is Euclidean distance between points x and y, sup and inf denote supremum and infimum.

Table 1
Imaging parameters and distinct patient population for each experiment are shown.

	PET	PET-CT	MRI-PET and MRI-PET-CT
# Patients	20	15	21
# Scans	20 PET	15 PET-CT	42 fused image: 21 MRI-PET and 21 PET-CT
Scanning parameters	$4 \times 4 \times 4$ mm^3	PET: $4 \times 4 \times 4$ mm^3 CT: $0.98 \times 0.98 \times 1.5$ mm^3	PET: $4.17 \times 4.17 \times 2.00$ mm^3 MRI: $1.11 \times 1.11 \times 7.8$ mm^3 CT: $1 \times 1 \times 1.5$ mm^3

Manual segmentations on all data were performed by three experts at three different time points (one week between each trial, and blinded among experts). We analyzed inter- and intra-observer agreements by DSC overlap ratios. Each expert was asked to segment the object of interest from PET only, CT only, MRI only, hybrid PET-CT, and hybrid MRI-PET images separately. Ground truth segmentations were constructed by averaging from these markings to obtain one final ground truth for each set of images. Fig. 4 summarizes inter- and intra-observer agreement rates. The agreement rates are higher when functional and anatomical images are used together in the manual segmentation. Compared to the segmentation of lesions from PET-CT images, MRI-PET images were segmented with higher global agreements, presumably due to their excellent soft-tissue contrast resolution.

3.2. Evaluation: Segmentation of PET images

In this subsection, we report the efficacy of the proposed co-segmentation algorithm in delineating uptake regions from PET images without incorporating anatomical information. To conduct a delineation process over uptake regions from PET images, we simply omit the anatomical terms in our proposed co-segmentation algorithm (i.e., $\alpha = \zeta = 0$, $\theta = \eta = 1$). Phantom and clinical PET images were used for validation and quantification of the segmentation results.

3.2.1. Validation by phantoms

Since ground truth images are usually difficult to obtain, phantoms are commonly used to evaluate the performance of segmentation algorithms, particularly in PET imaging. Phantom images
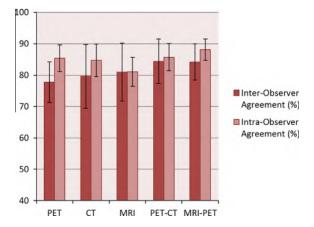

Fig. 4. Inter- and intra-observer agreements at manual segmentation are plotted for different imaging modalities. Observer agreement improves when functional and anatomical images are combined during tracing.

have the advantage of known true object boundary and can be compared to the delineation obtained by segmentation methods. To evaluate the efficacy of our proposed algorithm. we employed IEC image quality phantoms (NEMA, 1998). These phantoms contain six different spherical lesions of size 10, 13, 17, 22, 28, and 37 mm in diameter with two different signal to background ratios (SBRs) (i.e., 4:1 and 8:1), and two different voxel sizes (i.e., $2 \times 2 \times 2$ and $4 \times 4 \times 4$ mm^3) as reconstruction parameters. Fig. 5 shows the phantoms with different reconstruction parameters as well as ground truth (in (e)) simulated from CT. The proposed segmentation method was applied to these phantoms and evaluated by matching with the ground truth in CT images. The resultant dice scores are shown in Fig. 6. High DSC values confirm the robustness and the accuracy of the proposed delineation algorithm. It is noteworthy that low resolution and low SBRs degrade the delineation performance as expected. In all conditions, a DSC rate above 83% is observed. Performance of our proposed method is much higher when realistic PET image parameters (64 mm^3 with SBR ratio 8:1) are used with DSC rates above 90–95%, which is generally accepted as excellent.

3.2.2. Comparison to other methods

Although our main interest in this study is to delineate structures jointly from anatomical and functional images, we also show how well the proposed method performs on PET images alone when compared to the PET image segmentation methods commonly used in the literature. For this purpose, we implemented fixed and adaptive thresholding methods (Otsu, 1979), ITM (Jentzen et al., 2007), FCM (Zaidi et al., 2002; Belhassen and Zaidi, 2010), FLAB (Hatt et al., 2009), and region growing methods (Li et al., 2008; Day et al., 2009) and we particularly optimized these methods for the segmentation of PET images. Fig. 7 demonstrates an example PET image slice and segmentation results from those methods as well as our proposed method. Qualitative assessment of our proposed method (h) in comparison to others indicates that the proposed method is superior to other methods.

Quantitative evaluation of this comparison is depicted in Fig. 8, which demonstrates that the proposed method outperforms the best among these other methods based on the DSC scores over 20 subjects. Furthermore, region growing (f) and ITM (e) perform similarly and superior to FLAB (g) and other thresholding methods. Meanwhile, our method is also highly (perfectly) reproducible since automatically defined IURs allocate the foreground seeds in the same locations, and therefore the same boundary is obtained after delineation. In case when we have different foreground seed allocations, random walk segmentation was still shown to be less sensitive to seed localization among all graph based segmentation methods (Grady, 2006) (except fuzzy connectedness which provides a theoretical guarantee of robustness with respect to seeds). This is not the case for the above region growing method. Moreover, FLAB and thresholding methods require a precise ROI definition to remove false positives. This extra step inevitably increases the time for segmentation, and user interaction makes the whole process also subjective.

3.3. Evaluation: Co-segmentation of PET-CT images

Clinical PET-CT volumes obtained from 15 patients retrospectively collected were used to verify the efficacy of the co-segmentation algorithm. Each PET-CT scan had varying amounts of uptake in abnormal structures pertaining to different diseases. A total of 75 lesions from all patients were segmented automatically and compared to the ground truth markings. By following the RECIST criteria and to avoid any bias in the evaluations (Wahl et al., 2009), we selected no more than ten lesions from each patient for the quantification of delineations.
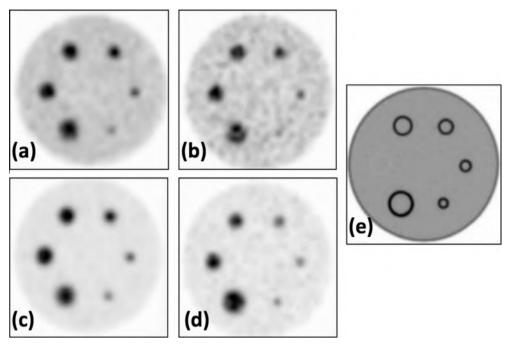
Fig. 5. PET phantom images (a–d) with CT acquisition ground truth (e). Phantoms have the following SBRs and voxel sizes: (a) 4:1, 8 mm^3, (b) 4:1, 64 mm^3, (c) 8:1, 8 mm^3, and (d) 8:1, 64 mm^3.
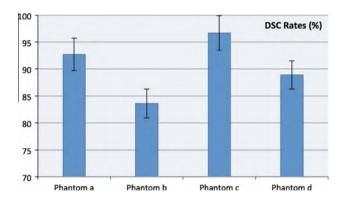

Fig. 6. DSC rates obtained over IEC phantoms (a–d). Phantoms have the following SBRs and voxel sizes: (a) 4:1, 8 mm^3, (b) 4:1, 64 mm^3, (c) 8:1, 8 mm^3, and (d) 8:1, 64 mm^3.

Fig. 9 shows some segmentation examples. Co-segmentation of PET-CT images (blue), segmentation of CT images (green), and PET images (yellow) are shown in first, second, and third columns, respectively. The fourth column reveals all segmentations overlaid together for comparison. In all images, ground truth segmentation is shown in black. Effective delineations were obtained by using the proposed co-segmentation method which appears qualitatively superior to the delineations obtained from using single image modality, i.e., CT or PET. The average DSCs and HDs of delineations over all 15 subjects and comparison to the method described in (Han et al., 2011) are displayed in Fig. 10. The proposed co-segmentation method yielded higher DSC scores and lower boundary mismatches on PET-CT images. A t-test showed that there was a statistically significant difference between the two methods (Han et al., 2011) ($p = 7.7e-10$).
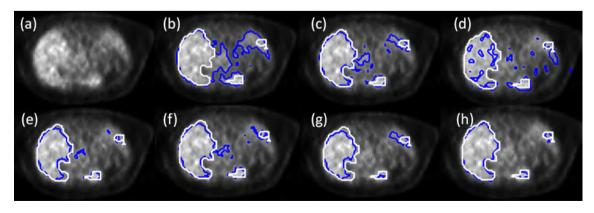

Fig. 7. Segmented uptake regions (blue) and ground truth (white) are shown for different segmentation methods for the PET image slice at (a). 40% fixed thresholding (b), 50% fixed thresholding (c), adaptive Otsu thresholding (d), ITM (e), region growing (f), FLAB (g), and our proposed method (h). (For interpretation of the references to color in this figure legend, the reader is referred to the web version of this article.)
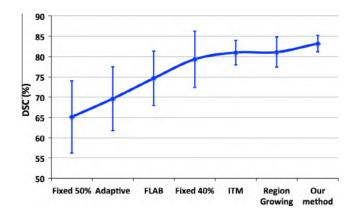
Fig. 8. DSC comparison of the proposed technique to the methods commonly used in the literature in segmentation of PET images. The proposed method is statistically significantly different from others ($p < 1.1e{-}4$ in all cases).

3.4. Evaluation: Co-segmentation of MRI-PET images

The recently established hybrid MRI-PET imaging is a preferred choice at present in clinical use over PET-CT because of several advantages of MRI over CT and since MRI-PET images provide new opportunities to quantify pathology and biochemical processes in vivo (Judenhofer et al., 2008). To the best of our knowledge, this is the first study quantifying anatomical and functional tissues jointly from MRI-PET scans. For the evaluation of segmentations, 21 IURs (all cancerous regions) were taken into consideration. Fig. 11 illustrates co-segmentation examples from PET-CT (a, b and c) and MRI-PET (d, e, and f) scans of the same patient. For simplicity, we demonstrate two observers' drawings (blue and green), and the co-segmentation results (white) overlaid on the same image (zoomed in c and f). In Fig. 11g, 3D rendered objects derived from PET-CT and MRI-PET segmentations are overlaid.

For quantitative evaluation, we display mean DSC and HD values in Fig. 12. MRI-PET co-segmentation produced more accurate delineations compared to delineations when either modality was used alone or when PET-CT was employed. Considering the fact that inter- and intra-observer variations are similar in PET-CT and MRI-PET reference segmentations, better performance of MRI-PET is probably due to better soft-tissue contrast of MRI.

3.5. Evaluation: Co-segmentation of fused MRI-PET-CT images

Registration of CT scans to MRI-PET scans: We fused CT images with MRI-PET scans via deformable image registration (Bagci and Bai, 2010; Bagci and Bai, 2008; Bagci and Bai, 2007). Since MRI has higher spatial resolution than CT and PET, and since MRI has already one-to-one spel correspondence with its PET counterpart, we registered CT scans to MRI scans to yield fused MRI-PET-CT images. For deformable registration, at most 20 K iterations were used during optimization. Moreover, we used nearly 700 K spatial samples from each modality (CT and MRI) to estimate mutual information histograms with 500 bins. The whole registration process takes an average of 13 s. Other registration methods such as elastic or diffeomorphic transformations (Geng et al., 2009; Gao et al., 2012) may also be used.

DSC and HD values for different scenarios are summerized in Figs. 13 and 14, respectively. Statistical comparison via a paired Student's t-test indicated that there were statistically significant differences in segmentations from PET-CT and MRI-PET ($p = 3.07e{-}9$), and PET-CT and MRI-PET-CT ($p = 4.42e{-}12$). There was no statistically significantly difference between MRI-PET and MRI-PET-CT if only DSC values are considered ($p = 0.18$). However, when HD values were considered, there was a statistically significant difference ($p = 4.89e{-}27$). Nevertheless, note that incorporating CT into MRI-PET scans slightly increases the DSC values and reduces the boundary mismatches significantly. One challenge in co-segmentation involving multiple modalities is that, since we do not have one-to-one correspondence for abnormal regions, it
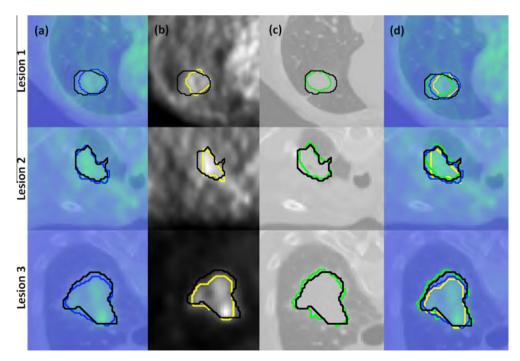

Fig. 9. Three different segmentation examples of uptake regions are shown in each column. First column: the proposed co-segmentation (blue) and ground truth (black) are overlaid. Second column: ground truth (black) and segmentation from PET only (yellow). Third column: ground truth (black) and segmentation from CT only (green). Fourth column: all segmentations and ground truth are overlaid together. (For interpretation of the references to color in this figure legend, the reader is referred to the web version of this article.)
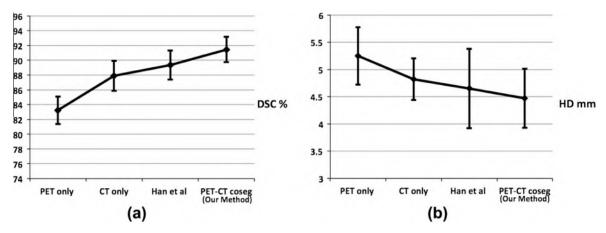
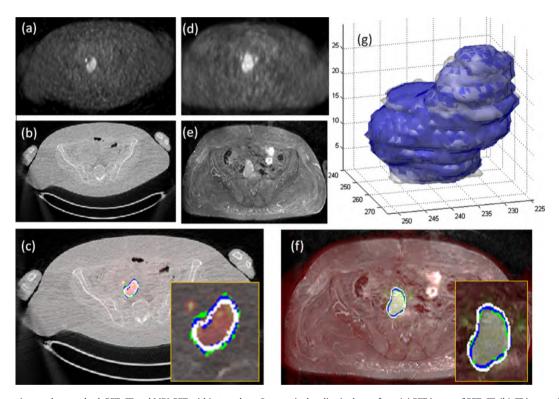**Fig. 10.** Mean DSCs (a) and HDs (b) are listed.

Fig. 11. The same patient underwent both PET-CT and MRI-PET within two days. One particular slice is shown from (a) PET image of PET-CT, (b) CT image of PET-CT, (c) PET-CT co-segmentation, (d) PET image of MRI-PET, (e) MRI image of MRI-PET scans is shown, and (f) MRI-PET co-segmentation. The proposed co-segmentation method jointly delineates uptake regions from PET images and abnormal tissue regions from corresponding structural images simultaneously (white lines in c and f). Two expert observers' drawings are shown as surrogate of truth (blue and green). Segmented regions from PET-CT and MRI-PET images are rendered and overlaid in (g) (white and blue, respectively). (For interpretation of the references to color in this figure legend, the reader is referred to the web version of this article.)

is not trivial to set the weighting factors of the imaging modalities before beginning delineation. We will discuss this issue in Section 3.7 in more detail.

3.6. Parameter selection for encoding function and the sensitivity of results to the size of the seed set

Image segmentation, the process of partitioning an image into distinctive subsets, as a whole can be thought of as consisting of two related tasks: recognition and delineation (Bagci et al., 2012c). While recognition is the process of determining roughly "where" the objects are and to distinguish them from other object-like entities in the image, delineation is the final step of defining the spatial extent of the object region/boundary in the image.

Computers are superior to humans in the delineation process while human recognition is superior to any other artificial recognition system assisted by computers. In seeded image segmentation methods, user defined seed localization is nothing but the recognition process. Similarly, our proposed detection algorithm is the recognition step for the segmentation process- "rough" object information is fed into the delineation process to make it fully automatic. In this case, "rough" object information is defined as the seed points (background and foreground). We achieve this rough identification process through an encoder function resembling thresholding with the variable N.

A definitive range of N is set with respect to the conventional values used in clinics such that SUV cut-off value of 2.5 (or 40–50% of SUV_{max}) corresponds to a sensitivity of 100% (Kara et al.,
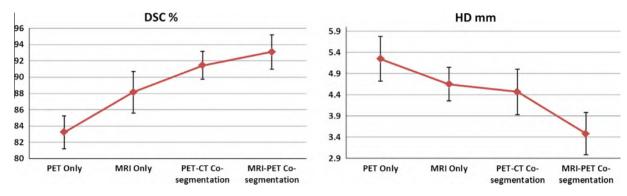
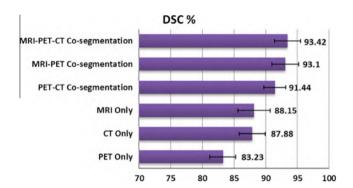**Fig. 12.** Mean DSCs (left) and HDs (right) are graphed. DSCs.

Fig. 13. Mean DSCs in the comparison of different scenarios.

2011). By following the assumption that 40–50% of SUV_{max} is of significance, N is selected to lie in the interval {2–2.5} in our implementation. Although our initial choice of N comes from this convention, N need not be restricted to the interval of {2–2.5}. In order to study how co-segmentation results are affected by the choice of N, we conducted PET-CT co-segmentation experiments with various N values. Fig. 15 plots the average DSC rates as a function of N, where the most accurate results were obtained when $N \approx 2$, in agreement with the clinical convention. Note also that average DSC rates are high and at clinically acceptable levels for $1.5 \leqslant N \leqslant 4$.

It is important to emphasize that our detection algorithm has a step where we insert additional background seeds into the spels lying on the spline connecting initial background seeds (step vi in Section 2.3), which offers more robustness to the segmentation algorithm in avoiding leakage. The procedure for inserting additional background seeds is depicted in Fig. 16. For each

foreground seed (yellow) in Fig. 16a, search in the 8 directions is conducted to find background seeds (red). Then, additional background seeds are added to this pool by selecting the spels lying on the spline connecting those background seeds in Fig. 16(b). We find this step necessary to avoid leakage in the delineation of the abnormal anatomy in structural images, particularly in CT scans, since abnormal and normal tissues can share similar intensity profiles. For instance, Fig. 17a illustrates an example of the leakage occurring due to the close proximity of normal and abnormal tissues with similar intensity profiles. The effect of additional background seeds on segmentation is shown in Fig. 17b. Seedings operations are done slice-by-slice. Furthermore, we have shown a few more seed detection examples in Fig. 18. Several convex and non-convex shaped uptake regions were successfully identified with foreground and background seeds as illustrated in different anatomical levels of different patients' PET scans in each column.

The detection part of the proposed computational framework becomes useful and critical particularly when there is a large number of uptake regions. In our experiments, for the smallest number of uptake regions over all data sets, our detection algorithm found 16 foreground and 87 background seeds (221 additional background seeds). On the other hand, for the highest number of uptake regions, the detection algorithm finds 398 foreground and 2740 background seeds (3324 additional background seeds). Automatic detection of IURs is accomplished within seconds. Despite the obvious advantages of the automated IUR detection algorithm, it may be also of interest for the clinicians to do manual seeding in order to constrain the region of interest to a certain part of the body especially when the number of IURs is small. Since some organs (brain, kidneys, and ureters) normally have high FDG uptakes even in the absence of pathology, a manual seeding based co-segmentation can be utilitarian. Accordingly, we designed the
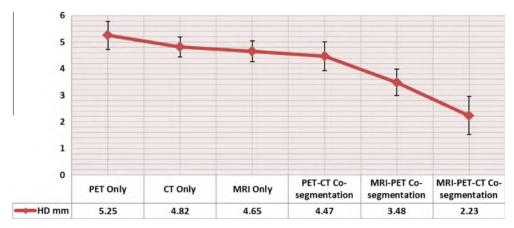

	PET Only	CT Only	MRI Only	PET-CT Co-segmentation	MRI-PET Co-segmentation	MRI-PET-CT Co-segmentation
HD mm	5.25	4.82	4.65	4.47	3.48	2.23

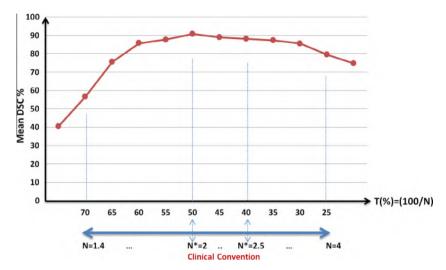**Fig. 14.** Mean HDs in the comparison of different scenarios.

Fig. 15. DSC values as a function of N in co-segmentation experiments conducted on PET-CT scans. The best DSC values are obtained when $N \approx 2$.
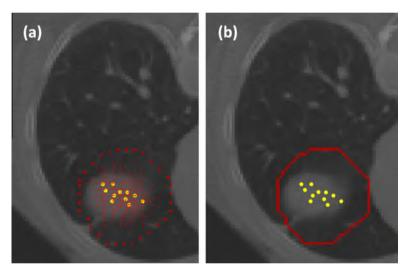

Fig. 16. (a) For each foreground seed (yellow), search in 8-directions is conducted to find the first corresponding background seeds (red). (b) These background seeds are connected through a spline curve and spels lying on the spline are also added to the pool of background seeds. (For interpretation of the references to color in this figure legend, the reader is referred to the web version of this article.)
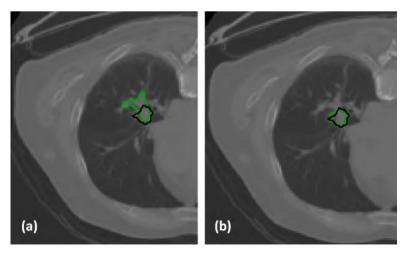

Fig. 17. Ground truth segmentation (black) and the random walk segmentation (green) with and without using additional background seeds are shown. (a) Leakage may occur due to the close proximity of normal and abnormal tissues when a limited number of background seeds was used. (b) Leakage can be avoided by using the additional background seeds. Seeds are obtained from PET correspondence of the CT scan. (For interpretation of the references to color in this figure legend, the reader is referred to the web version of this article.)
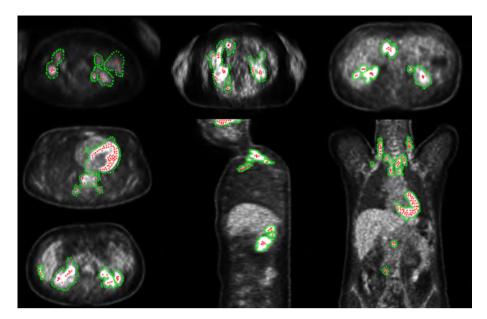
Fig. 18. Various seeding examples are shown for different anatomical levels from different subject's PET images. Red: foreground seeds, green: background seeds. (For interpretation of the references to color in this figure legend, the reader is referred to the web version of this article.)

co-segmentation software platform to provide both automated and manual seeding facilities. Since the co-segmentation method now involves the use of manual IUR identification as well, in parallel with the effect of the choice of N on co-segmentation in the previous experiment, sensitivity analysis of the method with respect to the total seed set is necessary. We analyzed the average DSC values of the resulting object boundaries using all MRI-PET-CT scans. Fig. 19 depicts the results. As is readily seen that the co-segmentation algorithm shows high robustness to seed quantity. Considering the fact that the number of seeds placed by the users is typically in the range of 20–40%, we may readily appreciate the advantages of the automatic detection of IURs. Note that once foreground seeds are placed manually, background seeds can either be found automatically by employing a search in 8-directions for each foreground seed, or they can be defined manually too. Sensitivity analysis of seed locations for a typical seed based random walk segmentation can be found elsewhere (Grady, 2006).

Fig. 19. Sensitivity analysis of the co-segmentation method with manual seeding.

3.7. Relationship between anatomical and functional regions

Sometimes it is appropriate to consider a one-to-one relationship between two different structural images of the same abnormal region. However, the assumption of identical lesion contours in both functional and structural images is questionable and unrealistic. For instance, depending on the functional characteristics of the cells within a lung tumor, it may not take up a radiotracer in all its volume, or uptake region may be larger than the anatomical boundary of the tumor due to cellular activation in nearby tissues. Furthermore, several clinical research studies have reported substantial anatomical and functional variations through different imaging modalities (Daisne et al., 2004; Roels et al., 2009). For example, tumor extension at the level of the lateral and posterior pharyngeal wall was depicted in CT, but not in MRI, and anatomical correspondence of the uptake region of the pharyngeal wall in PET images was considerably smaller (Daisne et al., 2004; Roels et al., 2009). For further demonstration, Fig. 20 shows MRI-PET images from different subjects to exemplify the variability between anatomical and functional structures' margins. In Fig. 20c and i, the left arrows indicate *almost* one-to-one correspondence between structural (b and h) and functional regions (a–g) regions. In the same images, right arrows show larger regions in functional images
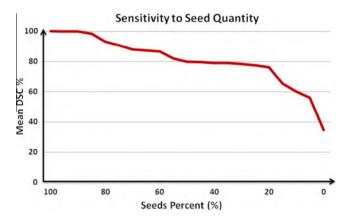
but smaller in anatomical correspondences. In contrast, in (d)–(f), a relatively smaller uptake but a larger anatomical correspondence region is seen.

Due to all these reasons and the variability between functional and anatomical regions reported extensively in the literature, we incorporated weight parameters into the co-segmentation method as earlier formulated in Section 2. In this Section, we explain further how our co-segmentation method was designed to mimic possible variability issue by introducing weighting parameters in the original graph construction. In Eq. (14), the combinatorial Laplacian matrices of the product graph include the weight parameters for MRI, CT, and PET as γ, α, and θ, and similarly in Eq. (15), initial probability distribution x^F of the product graph used the weighting parameters ξ, ζ, and η for MRI, CT, and PET, respectively. Anatomical and functional weight parameters can be set in two ways. First, ξ, ζ, and η can be considered equal for the computation of initial probability distribution combined from each modality, and then γ, α, and θ can be set properly based on the visibility of the abnormal regions from imaging modalities given that the summation of the variables are bounded, i.e., $\gamma + \alpha + \theta = 1$ and $0 \leqslant \gamma, \alpha, \theta \leqslant 1$. Second, γ, α, and θ can be considered as equal and then ξ, ζ, and η can be set similar to the first option.
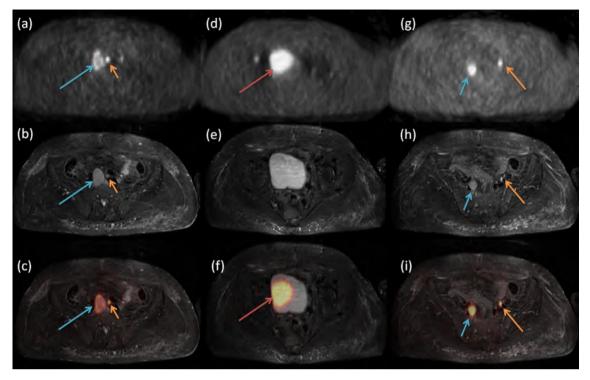
Fig. 20. Abnormal regions from anatomical and functional images may show low to high variations. PET, MRI, and PET-MRI images with small variability across scans (left arrow), and intermediate variability (right arrow) are shown in (a–c and g–i). Large variability between functional and anatomical structures is observed in (d–f). (For interpretation to colours in this figure, the reader is referred to the web version of this paper.)

In our experiments, the best possible combination of (α, θ) was found to be (0.2, 0.8) for PET-CT experiments, and (γ, θ) was found to be (0.3, 0.7) for MRI-PET experiments. Similarly, for MRI-PET-CT experiments, the best possible combination of (α, θ, γ) was found to be (0.2, 0.5, 0.3).

4. Concluding remarks

In this study, we showed the feasibility of noninvasive detection and accurate quantification of different types of pathologies via hybrid imaging modalities PET-CT and MRI-PET through a novel simultaneous joint segmentation method. Our proposed framework also included an automated pathology detection method, which helps the users in the identification of the object of interest and background regions automatically prior to delineation. We tested our method in both clinical and phantom data sets where PET, CT, PET-CT, MRI-PET, and finally MRI-PET-CT images were segmented to validate the intuition behind the co-segmentation idea. For PET image segmentation, we compared our method with the state-of-the-art methods, and also with another graph-based co-segmentation method applicable to PET-CT images with the assumption of one-to-one abnormal region correspondence between structural and functional images. In all cases, qualitative and quantitative comparisons showed that our proposed method achieves superior performance and may be used in clinical routine readily in the near future.

In this research, we employed the random walk method as the basic delineation engine. Its greatest strength is robustness against leakage. Consequently its weakness is the inability to encompass details, such as spiculations. On the other hand, fuzzy connectedness (FC) algorithms are strong in covering details. They are 100% robust relative to seeds, and are very efficient. Given enough seeds, as in our methods, therefore, it will be interesting to compare the two approaches on a larger cohort of data for their clinical efficacy.

Furthermore, we will explore the use of our automatic anatomy recognition systems (Bagci et al., 2012c; Chen et al., 2012; Udupa et al., 2011; Udupa et al., 2012) within the joint segmentation platform for improving automation.

References

Bagci, U., Bai, L., 2007. Multiresolution elastic medical image registration in standard intensity scale. In: SIBGRAPI XX Brazilian Symposium on Computer Graphics and Image Processing, pp. 305–312.

Bagci, U., Bai, L., 2008. Registration of standardized histological images in feature space. In: Proc. of SPIE Medical Imaging, pp. 69142V–1.

Bagci, U., Bai, L., 2010. Automatic best reference slice selection for smooth volume reconstruction of a mouse brain from histological images. IEEE Transactions on Medical Imaging 29, 1688–1696.

Bagci, U., Bray, M., Caban, J., Yao, J., Mollura, D., 2012a. Computer-assisted detection of infectious lung diseases: a review. Computerized Medical Imaging and Graphics 36, 72–84.

Bagci, U., Udupa, J., Yao, J., Mollura, D., 2012b. Co-segmentation of functional and anatomical images. In: Proc. of Medical Image Computing and Computer-Assisted Intervention, pp. 459–467.

Bagci, U., Chen, X., Udupa, J., 2012c. Hierarchical scale-based multi-object recognition of 3d anatomical structures. IEEE Transactions on Medical Imaging 31, 777–789.

Bagci, U., Yao, J., Caban, J., Turkbey, E., Aras, O., Mollura, D., 2011. A graph-theoretic approach for segmentation of pet images. In: Engineering in Medicine and Biology Society, EMBC, 2011 Annual International Conference of the IEEE. IEEE, pp. 8479–8482.

Basu, S., Kwee, T., Surti, S., Akin, E., Yoo, D., Alavi, A., 2011. Fundamentals of pet and pet/ct imaging. Annals of the New York Academy of Sciences 1228, 1–18.

Belhassen, S., Zaidi, H., 2010. A novel fuzzy c-means algorithm for unsupervised heterogeneous tumor quantification in pet. Medical Physics 37, 1309–1324.

Boellaard, R., Krak, N., Hoekstra, O., Lammertsma, A., 2004. Effects of noise, image resolution, and ROI definition on the accuracy of standard uptake values: a simulation study. Journal of Nuclear Medicine 45, 1519–1527.

Boudraa, A., Zaidi, H., 2006. Image segmentation techniques in nuclear medicine imaging. Quantitative Analysis in Nuclear Medicine Imaging, 308–357.

Bradley, J., Thorstad, W., Mutic, S., Miller, T., Dehdashti, F., Siegel, B., Bosch, W., Bertrand, R., 2004. Impact of FDG-pet on radiation therapy volume delineation in non-small-cell lung cancer. International Journal of Radiation Oncology, Biology and Physics 59, 78–86.

Brambilla, M., Matheoud, R., Secco, C., Loi, G., Krengli, M., Inglese, E., 2008. Threshold segmentation for pet target volume delineation in radiation treatment planning: the role of target-to-background ratio and target size. Medical Physics 35, 1207.

Brindle, K., 2007. New approaches for imaging tumour responses to treatment. Nature Reviews Cancer 8, 94–107.

Chen, X., Bagci, U., 2011. 3d automatic anatomy segmentation based on iterative graph cut asm. Medical Physics 38, 4610–4622.

Chen, X., Niemeijer, M., Zhang, L., Lee, K., Abramoff, M.D., Sonka, M., 2012. 3d segmentation of fluid-associated abnormalities in retinal oct: probability constrained graph-searchgraph-cut. IEEE Transactions on Medical Imaging 31, 1521–1531.

Chen, X., Udupa, J.K., Alavi, A., Torigian, D.A., 2010. Automatic anatomy recognition via multiobject oriented active shape models. Medical Physics 37, 6390–6401.

Chen, X., Udupa, J.K., Bagci, U., Zhuge, Y., Yao, J., 2011. Medical image segmentation by combining graph cut and oriented active appearance models. IEEE Transactions on Image Processing 21, 2035–2046.

Ciernik, I., Huser, M., Burger, C., Davis, J., Szekely, G., 2005. Automated functional image-guided radiation treatment planning for rectal cancer. International Journal of Radiation Oncology, Biology, and Physics 62, 893–900.

Cignoni, P., Rocchini, C., Scopigno, R., 1998. Metro: measuring error on simplified surfaces. Computer Graphics Forum 18, 167–174.

Cypess, A. et al., 2009. Identification and importance of brown adipose tissue in adult humans. The New England Journal of Medicine 360, 1509–1517.

Daisne, J., Duprez, T., Weynand, B., Lonneux, M., Hamoir, M., Reychler, H., Gregoire, V., 2004. Tumor volume in pharyngolaryngeal squamous cell carcinoma: comparison at ct, mr imaging, and fdg pet and validation with surgical specimen. Radiology 233, 93–100.

van Dalen, J., Hoffmann, A., Dicken, V., Vogel, W., Wiering, B., Ruers, T., Karssemeijer, N., Oyen, W., 2007. A novel iterative method for lesion delineation and volumetric quantification with fdg pet. Nuclear Medicine Communications 28, 485.

Davis, J., Reiner, B., Huser, M., Burger, C., Szekely, G., Ciernik, I., 2006. Assessment of 18f pet signals for automatic target volume definition in radiotherapy treatment planning. Radiotherapy and Oncology 80, 43–50.

Day, E., Betler, J., Parda, D., Reitz, B., Kirichenko, A., Mohammadi, S., Miften, M., 2009. A region growing method for tumor volume segmentation on pet images for rectal and anal cancer patients. Medical Physics 36, 4349.

Dice, L., 1945. Measures of the amount of ecologic association between species. Ecology 26, 297–302.

Drever, L., Roa, W., McEwan, A., Robinson, D., 2007. Iterative threshold segmentation for pet target volume delineation. Medical Physics 34, 1253.

Drever, L., Robinson, D., McEwan, A., Roa, W., 2006. A local contrast based approach to threshold segmentation for pet target volume delineation. Medical Physics 33, 1583.

El Naqa, I., Yang, D., Apte, A., Khullar, D., Mutic, S., Zheng, J., Bradley, J., Grigsby, P., Deasy, J., 2007. Concurrent multimodality image segmentation by active contours for radiotherapy treatment planning. Medical Physics 34, 4738.

Erasmus, J., Gladish, G., Broemeling, L., Sabloff, B., Truong, M., Herbst, R., Munden, R., 2003. Interobserver and intraobserver variability in measurement of non-small-cell carcinoma lung lesions: implications for assessment of tumor response. Journal of Clinical Oncology 21, 2574–2582.

Erdi, Y., Mawlawi, O., Larson, S., Imbriaco, M., Yeung, H., Finn, R., Humm, J., 1997. Segmentation of lung lesion volume by adaptive positron emission tomography image thresholding. Cancer 80, 2505–2509.

Erdi, Y., Rosenzweig, K., Erdi, A., Macapinlac, H., Hu, Y., Braban, L., Humm, J., Squire, O., Chui, C., Larson, S., et al., 2002. Radiotherapy treatment planning for patients with non-small cell lung cancer using positron emission tomography (pet). Radiotherapy and Oncology 62, 51–60.

Evanko, D., 2008. Two pictures are better than one. Nature Methods 5, 377.

Fahey, F., Kinahan, P., Doot, R., Kocak, M., Thurston, H., Poussaint, T., 2010. Variability in pet quantitation within a multicenter consortium. Medical Physics 37, 3660.

Fiorino, C., Reni, M., Bolognesi, A., Cattaneo, G., Calandrino, R., 1998. Intra-and inter-observer variability in contouring prostate and seminal vesicles: implications for conformal treatment planning. Radiotherapy and Oncology 47, 285–292.

Fletcher, J. et al., 2008. Recommendations on the use of 18f-fdg pet in oncology. Journal of Nuclear Medicine 49, 480–508.

Fox, J., Rengan, R., O'Meara, W., Yorke, E., Erdi, Y., Nehmeh, S., Leibel, S., Rosenzweig, K., 2005. Does registration of pet and planning ct images decrease interobserver and intraobserver variation in delineating tumor volumes for non-small-cell lung cancer? International Journal of Radiation Oncology, Biology, and Physics 62, 70–75.

Gao, Y., Rathi, Y., Bouix, S., Tannenbaum, A., 2012. Filtering in the diffeomorphism group and the registration of point sets. IEEE Transactions on Image Processing 21, 4283–4396.

Geets, X., Lee, J., Bol, A., Lonneux, M., Grégoire, V., 2007. A gradient-based method for segmenting fdg-pet images: methodology and validation. European Journal of Nuclear Medicine and Molecular Imaging 34, 1427–1438.

Geng, X., Christensen, G., Gu, H., Ross, T., Yang, Y., 2009. Implicit reference-based group-wise image registration and its application to structural and functional mri. NeuroImage 47, 1341–1351.

Grady, L., 2006. Random walks for image segmentation. IEEE Transactions on Pattern Analysis and Machine Intelligence 28, 1768–1783.

Han, D., Bayouth, J., Song, Q., Taurani, A., Sonka, M., Buatti, J., Wu, X., 2011. Globally optimal tumor segmentation in pet-ct images: a graph-based co-segmentation method. In: Inf Process Med Imaging, pp. 245–256.

Harary, F., 1994. Graph Theory. ABP.

Hatt, M., Cheze le Rest, C., Turzo, A., Roux, C., Visvikis, D., 2009. A fuzzy locally adaptive bayesian segmentation approach for volume determination in pet. IEEE Transactions on Medical Imaging 28, 881–893.

Jentzen, W., Freudenberg, L., Eising, E., Heinze, M., Brandau, W., Bockisch, A., 2007. Segmentation of pet volumes by iterative image thresholding. Journal of Nuclear Medicine 48, 108–114.

Judenhofer, M. et al., 2008. Simultaneous pet-mri: a new approach for functional and morphological imaging. Nature Medicine 14, 459–465.

Juweid, M., Cheson, B., 2006. Positron-emission tomography and assessment of cancer therapy. The New England Journal of Medicine 354, 496–507.

Kanakatte, A., Gubbi, J., Srinivasan, B., Mani, N., Kron, T., Binns, D., Palaniswami, M., 2008. Pulmonary tumor volume delineation in pet images using deformable models. In: Engineering in Medicine and Biology Society, 2008. EMBS 2008. 30th Annual International Conference of the IEEE. IEEE, pp. 3118–3121.

Kara, O., Kara, T., Karagedik, G., Sahin, O., Ceylan, E., Sari, O., 2011. The role of fluorodeoxyglucose-positron emission tomography/computed tomography in differentiating between benign and malignant adrenal lesions. Nuclear Medicine Communications 32, 106–112.

Kolmogorov, V., Boykov, Y., 2005. What metrics can be approximated by geo-cuts, or global optimization of length/area and flux. In: Proc. of ICCV, pp. 564–571.

Koshy, M., Paulino, A., Howell, R., Schuster, D., Halkar, R., Davis, L., 2005. F-18 fdg pet-ct fusion in radiotherapy treatment planning for head and neck cancer. Head & Neck 27, 494–502.

Li, H., Thorstad, W., Biehl, K., Laforest, R., Su, Y., Shoghi, K., Donnelly, E., Low, D., Lu, W., 2008. A novel pet tumor delineation method based on adaptive region-growing and dual-front active contours. Medical Physics 35, 3711.

Matheoud, R., Monica, P., Loi, G., Vigna, L., Krengli, M., Inglese, E., Brambilla, M., 2011. Influence of reconstruction settings on the performance of adaptive thresholding algorithms for fdg-pet image segmentation in radiotherapy planning. Journal of Applied Clinical Medical Physics, 12.

Miele, E. et al., 2008. Positron emission tomography (pet) radiotracers in oncology utility of 18f-fluoro-deoxy-glucose (fdg)-pet in the management of patients with non-small-cell lung cancer (nsclc). Journal of Experimental Clinical Research 27, 52.

NEMA, I.B.P.S., 1998. International Standard: Radionuclide Imaging Devices Characteristics and Test Conditions Part 1: Positron Emission Tomographs. Technical Report. International Electrotechnical Commission (IEC).

Nestle, U., Kremp, S., Grosu, A., 2006. Practical integration of 18f-fdg-pet and pet-ct in the planning of radiotherapy for non-small cell lung cancer (nsclc): The technical basis, icru-target volumes, problems, perspectives. Radiotherapy and Oncology 81, 209–225.

Otsu, N., 1979. A threshold selection method from gray-level histograms. IEEE Transactions on Systems, Man, and Cybernetics 9, 62–66.

Prieto, E., Lecumberri, P., Pagola, M., Gómez, M., Bilbao, I., Ecay, M., Peñuelas, I., Martí-Climent, J., 2012. Twelve automated thresholding methods for segmentation of pet images: a phantom study. Physics in Medicine and Biology 57, 3963.

Roels, S., Slagmolen, P., Nuyts, J., Lee, J., Loeckx, D., Maes, F., et al., 2009. Biological image-guided radiotherapy in rectal cancer: challenges and pitfalls. International Journal of Radiation Oncology, Biology, and Physics 75, 782–790.

Schaefer, A., Kremp, S., Hellwig, D., Rübe, C., Kirsch, C., Nestle, U., 2008. A contrast-oriented algorithm for fdg-pet-based delineation of tumour volumes for the radiotherapy of lung cancer: derivation from phantom measurements and validation in patient data. European Journal of Nuclear Medicine and Molecular Imaging 35, 1989–1999.

Schinagl, D., Vogel, W., Hoffmann, A., van Dalen, J., Oyen, W., Kaanders, J., 2007. Comparison of five segmentation tools for 18f-fluoro-deoxy-glucose-positron emission tomography-based target volume definition in head and neck cancer. International Journal of Radiation Oncology, Biology and Physics 69, 1282–1289.

Shankar, L., Hoffman, J., Bacharach, S., Graham, M., Karp, J., Lammertsma, A., Larson, S., Mankoff, D., Siegel, B., Van den Abbeele, A., et al., 2006. Consensus recommendations for the use of 18f-fdg pet as an indicator of therapeutic response in patients in national cancer institute trials. Journal of Nuclear Medicine 47, 1059–1066.

Thie, J., 2004. Understanding the standardized uptake value, its methods, and implications for usage. Journal of Nuclear Medicine 45, 1431–1434.

Udupa, J., Odhner, D., Falcao, A., Ciesielski, K., Miranda, P., Matsumoto, M., Grevera, G., Saboury, B., Torigian, D., 2012. Automatic anatomy recognition via fuzzy object models. In: SPIE Medical Imaging, SPIE. p. 8316.

Udupa, J., Odhner, D., Falcao, A., Ciesielski, K., Miranda, P., Vaideeswaran, P., Mishra, S., Grevera, G., Saboury, B., Torigian, D., 2011. Fuzzy object modeling. In: SPIE Medical Imaging, SPIE. p. 7964.

Van Baardwijk, A. et al., 2007. Pet-ct-based auto-contouring in non-small-cell lung cancer correlates with pathology and reduces interobserver variability in the delineation of the primary tumor and involved nodal volumes. International Journal of Radiation Oncology, Biology, and Physics 68, 771–778.

Vees, H., Senthamizhchelvan, S., Miralbell, R., Weber, D., Ratib, O., Zaidi, H., 2009. Assessment of various strategies for 18-f-fet pet-guided delineation of target volumes in high-grade glioma patients. European Journal of Nuclear Medicine and Molecular Imaging 36, 182–193.

Wahl, R., Jacene, H., Kasamon, Y., Lodge, M., 2009. From recist to percist: evolving considerations for pet response criteria in solid tumors. Journal of Nuclear Medicine 50, 122S–150S.

Yang, F., Grigsby, P., 2012. Delineation of fdg-pet tumors from heterogeneous background using spectral clustering. European Journal of Radiology.

Yu, H. et al., 2009. Coregistered fdg pet/ct-based textural characterization of head and neck cancer for radiation treatment planning. IEEE Transactions on Medical Imaging 28, 373–383.

Zaidi, H., Diaz-Gomez, M., Boudraa, A., Slosman, D., 2002. Fuzzy clustering-based segmented attenuation correction in whole-body pet imaging. Physics in Medicine and Biology 47, 1143.

Zaidi, H., El Naqa, I., 2010. Pet-guided delineation of radiation therapy treatment volumes: a survey of image segmentation techniques. European Journal of Nuclear Medicine and Molecular Imaging 37, 2165–2187.